PAPER • OPEN ACCESS

The three-dimensional equilibrium with magnetic islands and MHD instabilities in the CFQS quasi-axisymmetric stellarator

To cite this article: X.Q. Wang *et al* 2021 *Nucl. Fusion* **61** 036021

OPEN ACCESS
IOP Publishing | International Atomic Energy Agency Nuclear Fusion

Nucl. Fusion **61** (2021) 036021 (8pp) https://doi.org/10.1088/1741-4326/abd3ec

The three-dimensional equilibrium with magnetic islands and MHD instabilities in the CFQS quasi-axisymmetric stellarator

X.Q. Wang[1], Y. Xu[1], A. Shimizu[2], M. Isobe[2,3], S. Okamura[2], Y. Todo[2], H. Wang[2], H.F. Liu[1], J. Huang[1], X. Zhang[1], H. Liu[1], J. Cheng[1], C.J. Tang[4] and the CFQS team

[1] Institute of Fusion Science, School of Physical Science and Technology Southwest Jiaotong University, Chengdu 610031, China
[2] National Institute for Fusion Science, National Institutes of Natural Sciences, Toki, Gifu 509-5292, Japan
[3] SOKENDAI (The Graduate University for Advanced Studies), Toki, Gifu 509-5292, Japan
[4] School of Physical Science and Technology, Sichuan University, Chengdu 610041, China

E-mail: xuyuhong@swjtu.edu.cn

Received 8 July 2020, revised 11 December 2020
Accepted for publication 15 December 2020
Published 15 February 2021

Abstract

The equilibrium of the Chinese first quasi-axisymmetric stellarator (CFQS) has been investigated by the HINT code. It is found that the stochastization of magnetic field lines expands with the increase in the volume-averaged beta value $\langle\beta\rangle$ in the plasma boundary. In the high-β regime, the generation of large magnetic islands at rational surfaces not only leads to an effective shrinkage of the plasma confinement region but also increases the outward shift of the magnetic axis. With bootstrap current effects, the low-order islands spread over the whole plasma area, leading to a stochastization of magnetic field lines due to island chain overlapping. However, for a flat pressure profile, the magnetic islands are significantly suppressed so that the magnetic surfaces can be fairly maintained. Moreover, the magnetohydrodynamic (MHD) instabilities in the optimized CFQS configurations have been simulated by the MEGA code. The linear properties of unstable resistive MHD modes are studied. The results show that in the CFQS the main MHD behaviour is dominated by the resistive ballooning modes with strong mode coupling. The mode structure and resistivity scaling are consistent with related theories.

Keywords: stellarator, three-dimensional equilibrium, quasi-axisymmetric stellarator, magnetic island, bootstrap current, stochastic magnetic field lines, magnetohydrodynamics

(Some figures may appear in colour only in the online journal)

1. Introduction

A quasi-axisymmetric stellarator (QAS) [1], as one type of optimized stellarator, has been widely studied in the past. In the QAS, neoclassical transport properties are similar to those in tokamaks, while there is no requirement for the inductively driven current. Therefore, the QAS is a three-dimensional (3D) tokamak-like device that combines the advantages of stellarators and tokamaks [1, 2]. To explore the potential merits of the advanced stellarator configuration, several devices with quasi-axisymmetric features have been designed, such as the compact helical system (CHS)-qa [3–7], the National Compact Stellarator Experiment [8–11] and the Evolutive Stellarator of Lorraine [12, 13].

Currently, a new compact QAS, the Chinese first quasi-axisymmetric stellarator (CFQS) is being designed as a joint project between Southwest Jiaotong University in China and the National Institute for Fusion Science in Japan [14]. The details of the CFQS design have been introduced in recent publications [15–19]. The basic parameters are as follows: the toroidal magnetic field $B_t = 1.0$ T, the major radius $R = 1.0$ m, the aspect ratio $A = 4.0$ and the toroidal periodic number $N_p = 2$.

In [15, 17], the magnetohydrodynamic (MHD) equilibrium of the CFQS with (or without) bootstrap currents has been calculated using the VMEC code [20], which is based on the assumption of perfect nested flux surfaces. However, in the QAS configuration, magnetic islands and the stochastization of field lines due to overlapping of island chains can naturally exist in the 3D MHD equilibrium [21], in particular, in the high-β regime with substantial bootstrap currents [17, 22]. As a consequence, the destruction of the nested magnetic flux surfaces is unavoidable. Therefore, it is necessary to calculate the CFQS equilibrium, including magnetic islands, for a good understanding of the basic properties of the QAS in finite plasma beta cases. Moreover, investigation of the magnetic topology near the plasma edge is also important for evaluating plasma confinement properties. For these purposes, in the present study we have calculated the free-boundary equilibrium of the CFQS with finite plasma pressure and currents using the HINT code [21].

On the other hand, in the QAS configuration with a low-aspect ratio, the bootstrap current is usually substantial, and hence, the MHD instabilities could be stronger than those in other stellarator configurations. We therefore perform the nonlinear MHD simulation for the typical configuration of the CFQS by the MEGA code [23]. The growth rate and spatial structure of the modes with finite plasma dissipation are discussed in detail.

The rest of this paper is organized as follows. In section 2, the equilibria with magnetic islands using the HINT code are discussed. Section 3 presents the simulations and analyses of the MHD stability. Finally, a summary is given in section 4.

2. Calculations of the CFQS equilibrium

HINT is a 3D MHD equilibrium code that uses the relaxation method without requiring nested flux surfaces like the VMEC code [20]. A brief introduction to this code has been given in [21]. In the new version of the HINT code, the cylindrical coordinate (R, ϕ, Z) is used with a high numerical accuracy. The single-fluid nonlinear MHD equations are solved using the relaxation method [24, 25]. The relaxation consists of two steps: (i) plasma pressure relaxation; and (ii) magnetic field relaxation. In step one, the magnetic field $\mathbf{B}$ is fixed and the plasma pressure (p) is calculated by $\mathbf{B} \cdot \nabla p = 0$. For the second step, the magnetic field is calculated by reduced MHD equations as

$$\frac{\partial \mathbf{v}}{\partial t} = -\nabla p + \left(\mathbf{j} - \mathbf{j}_0\right) \times \mathbf{B}, \tag{1}$$

$$\frac{\partial \mathbf{B}}{\partial t} = \nabla \times \left[(\mathbf{v} \times \mathbf{B}) - \eta \left(\mathbf{j} - \mathbf{j}_0 - \mathbf{j}_{\text{net}}\right)\right], \tag{2}$$

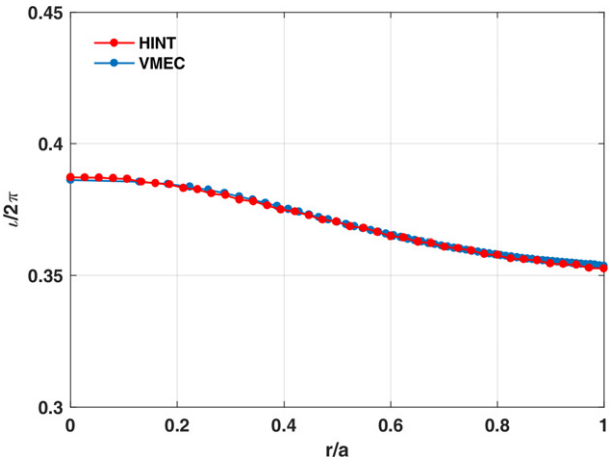

Figure 1. Comparison of the radial dependence of the rotational transform, $\iota/2\pi$, in the vacuum case between the HINT (red) and VMEC (blue) codes.

where the plasma pressure comes from the result of step one, t is the time, $\mathbf{v}$ is the plasma velocity, $\mathbf{j} = \nabla \times \mathbf{B}$ is the total current density, $\mathbf{j}_0$ is the initial current density, $\mathbf{j}_{\text{net}}$ is the net toroidal current like the bootstrap current, η is the dissipative parameter and the plasma density is assumed to be a constant.

In this section, typical configurations of the CFQS are calculated by the HINT code. For a benchmark between the HINT and VMEC codes, we have computed the rotational transform, $\iota/2\pi$, in the vacuum case for the CFQS using the two codes. The results are shown in figure 1. It can be seen that the free-boundary equilibrium obtained by the VMEC code is in good agreement with that by the HINT code in the case of without plasma. In such a scenario, the rotational transform between $\iota/2\pi = 2/6$ and $2/5$ avoids the low-order rational surfaces with a relatively weak magnetic shear.

After the benchmark, we further calculated the equilibrium with finite beta ($\langle\beta\rangle$ is volume-averaged) for the CFQS using the HINT code without considering the effects of the bootstrap current. The Poincaré plots of magnetic surfaces are illustrated in figure 2. In the calculation, the pressure profile, $p = p_0(1 - \psi)^2$, is employed with p_0 being the plasma pressure on the axis and ψ being the toroidal flux. It is shown that the ergodization of magnetic surfaces due to overlapping of island chains is enhanced with the increase in $\langle\beta\rangle$ at the plasma boundary. The reasons may be as follows: the increase in $\langle\beta\rangle$ induces changes in the iota profile, which generates a lot of low-order rational surfaces and, consequently, the island chains. Then, the overlap of the island chains results in stochastization of field lines at the plasma boundary and shrinkage of nested magnetic flux surfaces. From this point of view, in contrast to the situation in tokamaks, in stellarators the intrinsic 3D magnetic configuration may induce the generation of islands, even in vacuum fields, i.e. without any plasma or equilibrium response, because the field components may interact resonantly with field lines which have the appropriate rational value of the rotational transform. It should be noted that under the present CFQS configuration the magnetic surfaces can still be well maintained until $\langle\beta\rangle$ is larger than 1.4%, as shown

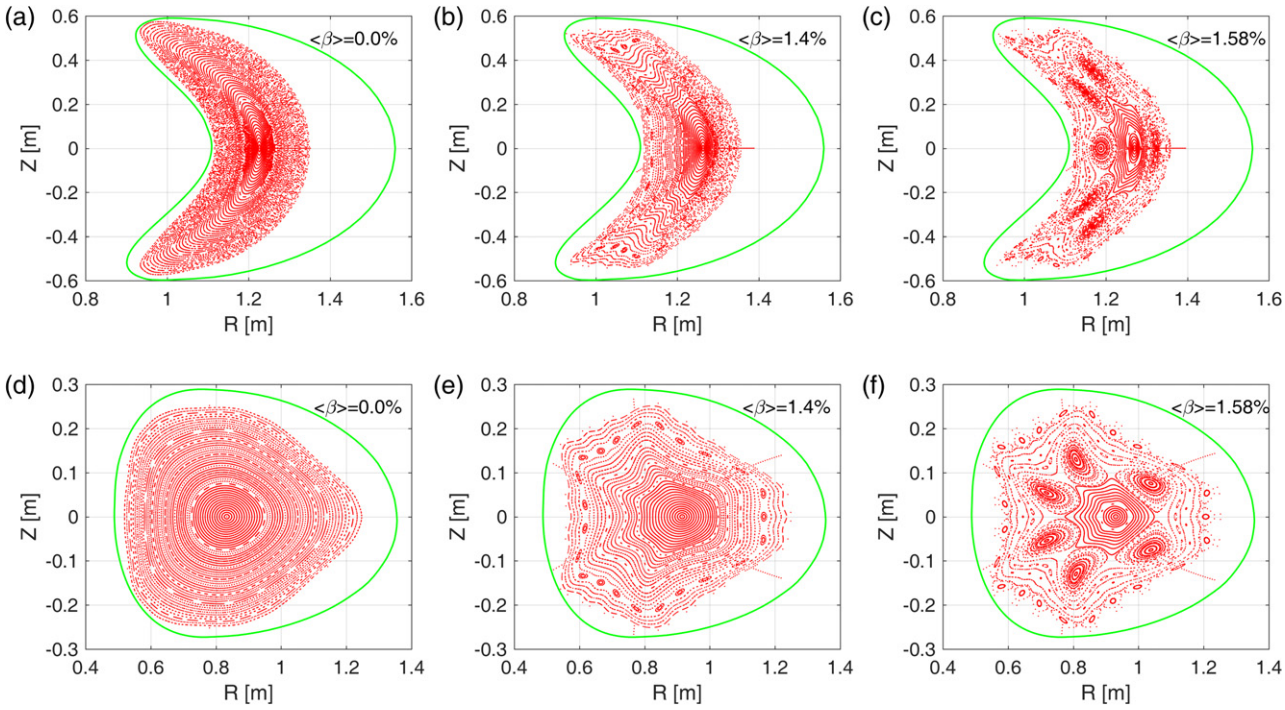

Figure 2. Poincaré plots of magnetic surfaces for different volume-averaged beta values ($\langle\beta\rangle = 0.0\%, 1.4\%, 1.58\%$) at two toroidal angles (a)–(c) $\phi = 0°$ and (d)–(f) $\phi = 90°$. The green line denotes the boundary of the vacuum vessel.

in figures 2(b) and (e). It has been proposed that, to reduce the deformation of the magnetic flux surfaces in the CFQS, in addition to 16 modular coils, external auxiliary coils with appropriate currents should be employed in high $\langle\beta\rangle$ cases [19]. Recently, Kinoshita *et al* reported the additional coil systems of the CFQS, including poloidal field coils to control the plasma position and shape and toroidal field coils to control the iota profile [19], which support a possible way to achieve an island divertor configuration for the CFQS [26].

To gain insight into the dependence of the magnetic axis position on the $\langle\beta\rangle$ value, the average positions of the magnetic axis are calculated by the HINT and VMEC codes for different $\langle\beta\rangle$. The results are shown in figure 3, where $R_{\rm ax}$ is the average position of the magnetic axis in the major radius direction. It can be seen that within the range of $\langle\beta\rangle \leqslant 1.4\%$ both the HINT and VMEC calculations show good consistency, and the $R_{\rm ax}$ increases almost linearly with increasing $\langle\beta\rangle$. However, when $\langle\beta\rangle$ is larger than $\sim$1.4%, the increase in the magnetic axis shift estimated by HINT is faster than that by VMEC. The possible reason is that in the calculation of HINT the $\iota/2\pi = 2/6$ island chains emerge, which may play a pushing role for an outward shift on the magnetic axis. This point can also be seen in figures 2(c) and (f), where four larger islands appear on the left side of the magnetic axis, while on the right side there are only two islands.

In the quasi-axisymmetric magnetic configuration of the CFQS, a substantial bootstrap current can be present in the high-β regime [17, 18]. Therefore, the equilibrium, including bootstrap currents, should be calculated to explore the configuration properties. In this work, the bootstrap current was estimated using the BOOTSJ code based on the drift kinetic model, as described in [27]. The calculations were iterated

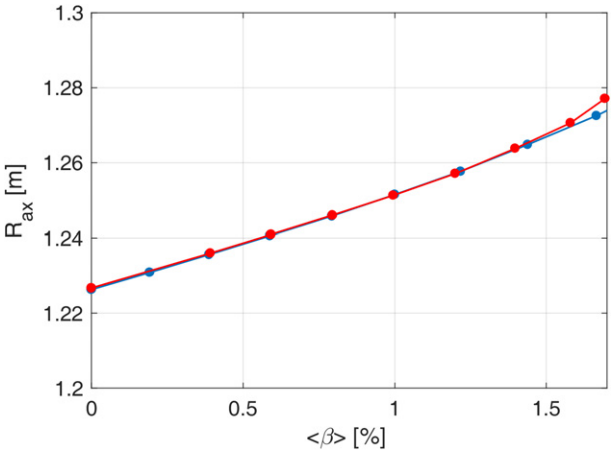

Figure 3. The average position of the magnetic axis in the major radius direction, $R_{\rm ax}$, as a function of $\langle\beta\rangle$ calculated by the HINT (red line) and VMEC (blue line) codes.

many times until the BOOTSJ calculation based on the equilibrium with bootstrap currents results in the same bootstrap current profile so that the final bootstrap current profiles and amplitudes are convergent.

To study the effects of the bootstrap current, we consider two cases of the density profile, i.e. case 1: the parabolic density profile $n(\psi) = n(0) \cdot (1 - \psi)$ and case 2: the flat density profile $n(\psi) = n(0) \cdot (1 - 0.8\psi + 1.3\psi^2 - 1.5\psi^3)$. The form of the flat density profile has been widely used for CHS [22], CHS-qa [22, 28] and CFQS [17] when evaluating the bootstrap current effects. In this work, to focus on the profile effect, the central electron and ion densities on the axis are fixed as $n_{\rm e}(0) = n_{\rm i}(0) = 10^{19}$ m^{-3}. The electron and ion temperature

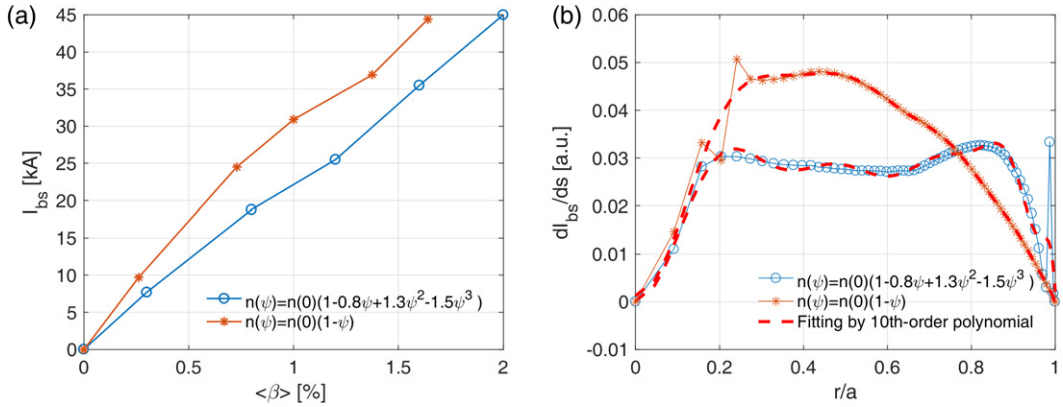

Figure 4. (*a*) The bootstrap current (I_{bs}) as a function of $\langle\beta\rangle$, and (*b*) the radial profile of the bootstrap current density (dI_{bs}/ds) at $\langle\beta\rangle \approx 1\%$ for the parabolic density profile (case 1) and the flat density profile (case 2) calculated by the BOOTSJ code. The dashed lines in figure 4(*b*) are the best fitting of the tenth-order polynomial.

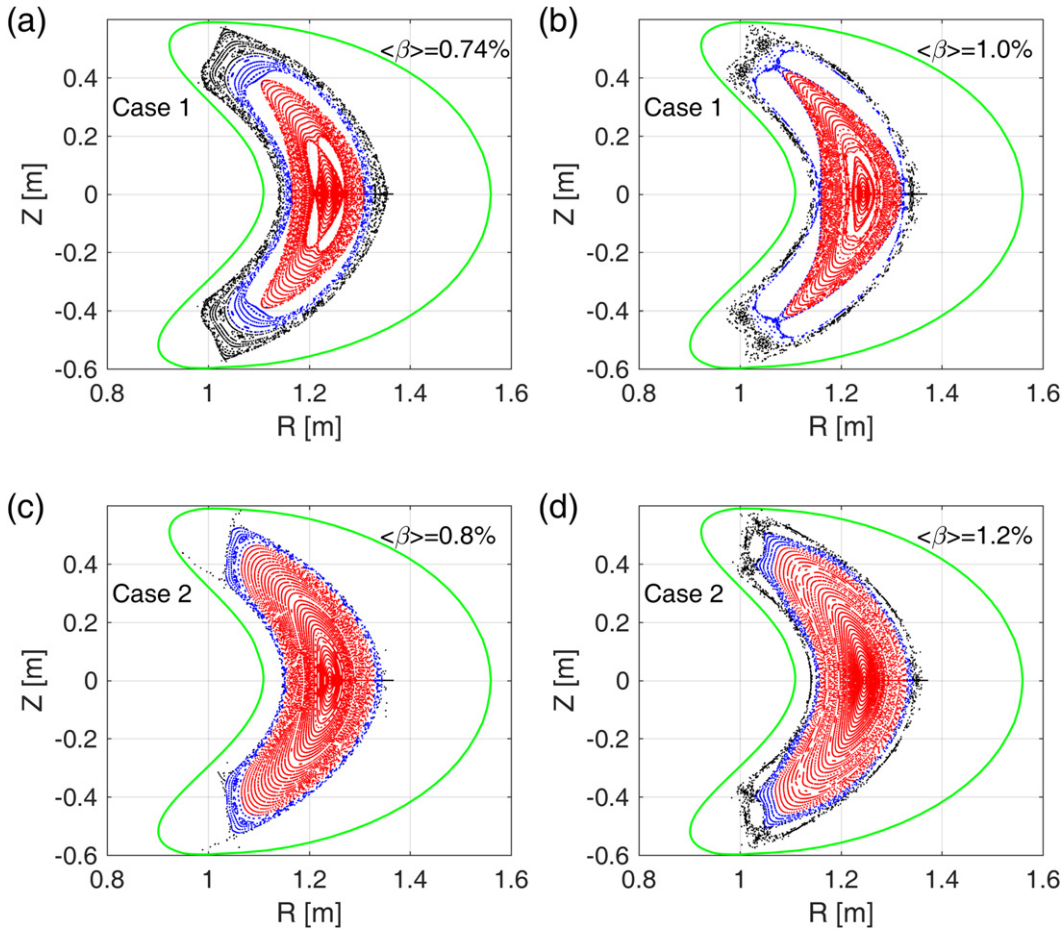

Figure 5. Poincaré plots of magnetic surfaces for (*a*) and (*b*) case 1 and (*c*) and (*d*) case 2 at different $\langle\beta\rangle$ values, where the black, blue and red colours mark the regions of $p/p_0 < 1\%$, $1\% \leqslant p/p_0 \leqslant 10\%$, and $p/p_0 > 10\%$, respectively. The green line denotes the boundary of the vacuum vessel.

profiles are $T_e(\psi) = T_e(0) \cdot (1-\psi)$ and $T_i(\psi) = T_i(0) \cdot (1-\psi)$ with $T_i(0) = 0.75T_e(0)$. The central values of the temperature depend on central plasma beta (or pressure) values. For example, in figure 4 for a central beta value $\beta_0 = 2.5\%$ with $B_t = 1.0$ T, $T_e(0) = 3.55$ keV and $T_i(0) = 2.66$ keV. From figures 4(*a*) and (*b*), we can see that a flat density profile can effectively reduce the amplitude of bootstrap currents and change the current density profile significantly. For the present CFQS design of $\langle\beta\rangle \sim 1\%$, the amplitude of the bootstrap current (I_{bs}) is about 30 kA and 20 kA for cases 1 and 2,

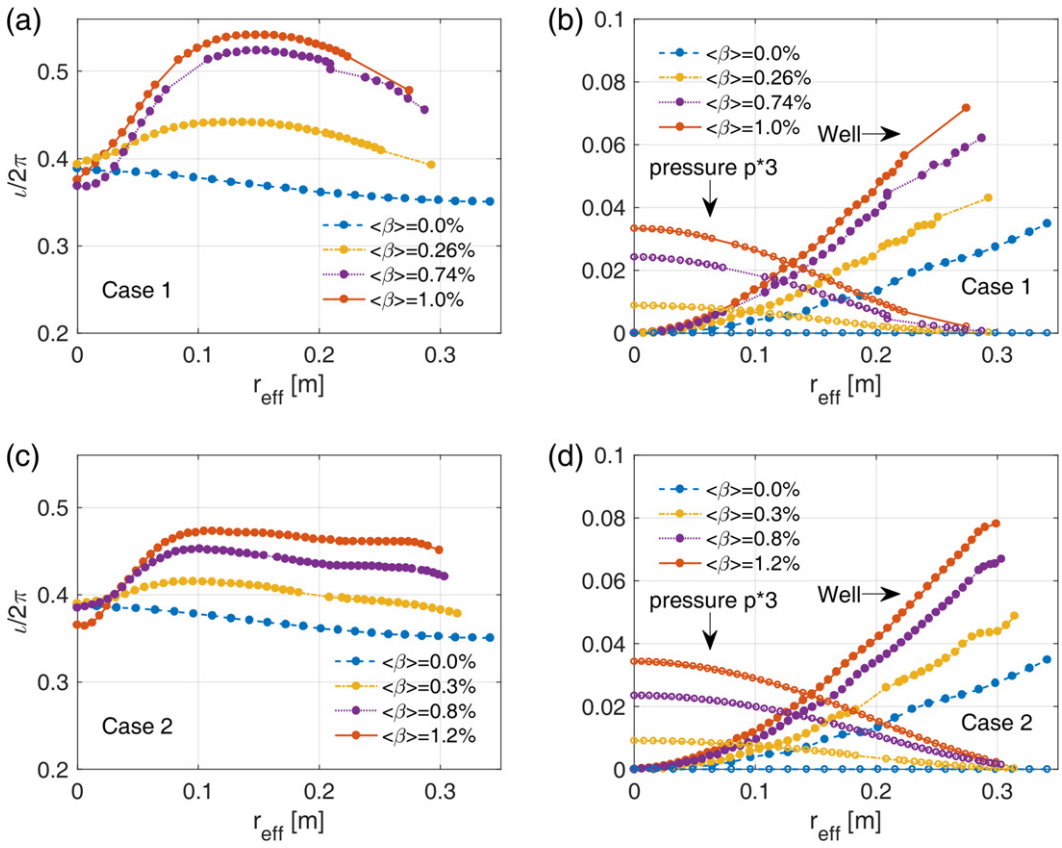

Figure 6. The rotational transform, magnetic well depth and plasma pressure as a function of the effective radius ($r_{\rm eff}$): (a) and (b) case 1 and (c) and (d) case 2 for different $\langle\beta\rangle$ values.

respectively. It is interesting to note that in case 1, the profile of the bootstrap current density ($\mathrm{d}I_{\rm bs}/\mathrm{d}s$) has a peak in the range of $r/a \approx (0.3–0.6)$, which may result in a reversed magnetic shear in the bulk plasma, whereas in case 2 the flat profile of $\mathrm{d}I_{\rm bs}/\mathrm{d}s$ in the central region suggests a locally weak magnetic shear. It should be noted that the spikes in the current profiles occur when the rotational transform crosses low-order rational surfaces.

To further survey the properties of islands in the QAS, we have calculated the equilibria of the CFQS with the bootstrap current using the HINT code. The Poincaré plots of magnetic surfaces are depicted in figure 5 for cases 1 and 2, where the black, blue and red colours mark the region of $p/p_0 < 1\%$, $1\% \leqslant p/p_0 \leqslant 10\%$, and $p/p_0 > 10\%$, respectively. The related parameters used in this figure are the same as we used in figure 4. For case 1, figures 5(a) and (b) show that with increasing beta from 0.74% to 1% the widths of the 2/4 island and 4/9 island chains both increase so that the space between these two island chains becomes smaller. Thus, the island chains connected to intermediate rationals, in particular 6/13 and 8/17 islands, grow as well and their overlap contributes to the generation of the stochastic region between the 4/9 and 2/4 islands. For case 2, as shown in figures 5(c) and (d), the magnetic islands and the field line stochastization are remarkably suppressed in comparison with case 1. In such a scenario the iota profiles do not contain the $\iota/2\pi = 2/4$ resonance, and hence, a 2/4 island cannot appear in the magnetic topology of the field. Although the boundary 4/9 island chain remains, the good flux surfaces are still kept over the entire plasma area. Furthermore, the 4/9 island chains in cases 1 and 2 exhibit different island phases, which is possibly due to different distributions of equilibrium currents and net currents in the two calculations. These results offer a possible prediction for the high-β equilibrium of the CFQS and suggest that the high-β operation scenarios can be realized if density profiles can be controlled by the electron cyclotron resonance heating, pellet injection and so on. Besides, a change in the temperature profiles may also serve the same goal.

In previous studies, it has been reported that the rotational transform and the magnetic well depth can be enhanced by increasing the bootstrap current in the QAS [22]. To identify the dependence of rotational transforms on bootstrap currents, the iota profiles and magnetic well depths for different $\langle\beta\rangle$ values are calculated and plotted in figure 6 as a function of the effective radius ($r_{\rm eff} = \sqrt{S/\pi}$), where S is the averaged areas of the poloidal cross section [25]. Here, the magnetic well depth is defined by $(V_{\rm p}'(0) - V_{\rm p}'(a))/V_{\rm p}'(0)$ for the QAS [22], where $V_{\rm p}$ is the plasma volume and prime denotes the derivative with respect to the toroidal flux.

For case 1, we can see that the iota values can cross 0.4 or 0.5 when the $\langle\beta\rangle$ is high enough. The increase in the iota value results from enhanced bootstrap currents. With the increase in $\langle\beta\rangle$, the iota profile changes from monotonic to non-monotonic, indicating a transition from a weak to a

reversed magnetic shear. It is also found that the iota values are rather sensitive to $\langle\beta\rangle$, especially in the low $\langle\beta\rangle$ cases. In the case of $\langle\beta\rangle \approx (0.7\%–1\%)$, the double iota = 2/4 rational surfaces are formed, which may trigger a fast-growing double kink/tearing instability. Figure 6(*b*) further indicates that with the increase in $\langle\beta\rangle$, the value of the magnetic well depth increases from 0% to 4.5% at the last closed flux surface ($r_{\rm eff} \approx 0.2$).

For case 2, it is also interesting to find that most of the iota profiles do not cross rational surfaces because of the small amplitude of the bootstrap current in comparison with case 1. This is the main reason why the good flux surfaces can be kept in such a case, as shown in figures 5(*c*) and (*d*). At a higher beta, the magnetic well profile in the radial range $r_{\rm eff} \lesssim 0.2$ m increases slightly faster in case 1 than that in case 2, which may result from the different peaking of the pressure profiles in the real space of the final HINT equilibria due to the changes in the magnetic configuration in the outer region. This point is confirmed by the final pressure distributions plotted in figures 6(*b*) and (*d*).

3. MHD stability analysis

The study of MHD instabilities is essential in the evaluation of the basic properties of QAS configurations; in particular, the ideal instabilities, including the kink and ballooning modes, have attracted close attention in the physical design and optimization of the QAS [5, 28, 29]. As an initial value MHD code, the MEGA code is a powerful tool for studying nonlinear MHD instabilities in 3D tokamaks and stellarators [23, 30, 31]. Therefore, in this work, simulations of global MHD stabilities have been carried out by the MEGA code for case 2 and the equilibrium configurations calculated in section 2 with $\langle\beta\rangle$=1.2% are used. In the simulation, the potential MHD instabilities are considered self-consistently by adopting an initial random perturbation. The plasma viscosity and diffusion coefficients are set to be 10^{-5} to maintain the numerical stability. The plasma resistivity, η, is taken to be 5×10^{-5} (unless stated in other specific cases). The growth rate and frequency of the modes are normalized by the Alfvén frequency ($\omega_{\rm A}$) in the equilibrium of case 2 in which the Alfvén time is $\sim 1.4 \times 10^{-7}$ s with the plasma density being 1×10^{19} m^{-3}. A Boozer coordinate system of the equilibrium was constructed for the spectral analysis of the simulation results [31].

The radial eigenmode structures of the unstable modes, with the dominant toroidal mode number $n = -4$ and the poloidal mode number $m = 0$–10, are shown in figure 7, where the radial velocity ($v_{\rm r}$) is normalized to the Alfvén velocity $v_{\rm A}$. The dominant mode numbers ($n = -4$ and $m = 8$, 9 and 10) are related to the rational values 4/8 (=1/2), 4/9 and 4/10 (=2/5). The peaking locations are all near the rational surface of 1/2 and also close to the weak shear regions, as shown in figure 6(*c*). It is clear that the radial structure shows a strong mode coupling around the same location.

Considering the important role of the plasma resistivity in its effect on MHD instabilities, we have calculated the dependence of the mode growth rate on the resistivity. The results

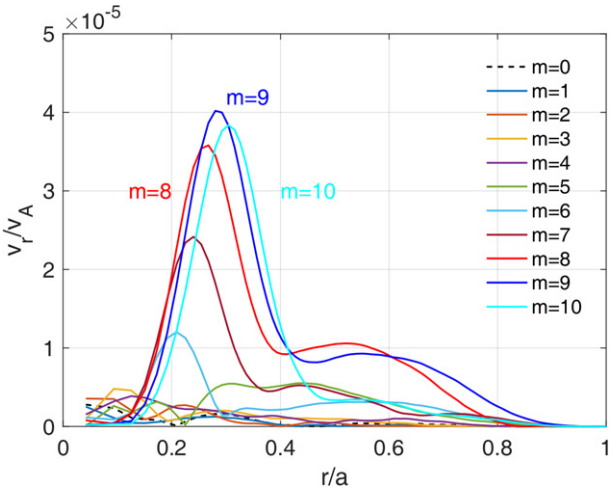

Figure 7. The radial profiles of the normalized radial velocity for $m = 0$–10 and $n = -4$.

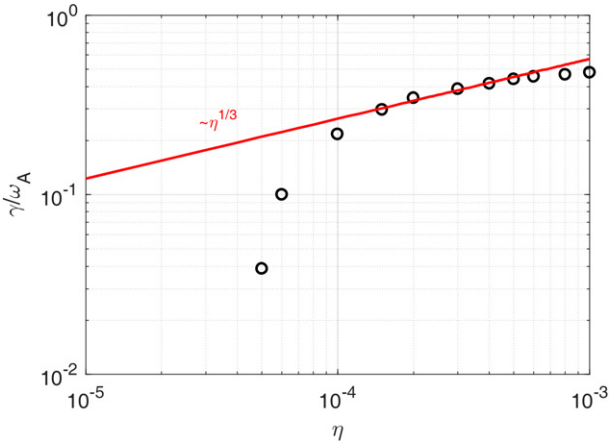

Figure 8. The linear growth rate of the mode, $\gamma = {\rm d}(\ln E_{\rm k})/{\rm d}t$, as a function of plasma resistivity and the fitting by $\eta^{1/3}$ with $\langle\beta\rangle \sim 1.2\%$.

are shown in figure 8, where the linear growth rate defined by $\gamma = {\rm d}(\ln E_{\rm k})/{\rm d}t$ and $E_{\rm k}$ is the kinetic energy. It can be seen that, for the high-η regimes of $\eta > 10^{-4}$, the mode is unstable. For the low-η regimes of $\eta < 10^{-5}$, the mode is stabilized. In the region of $10^{-4} < \eta < 10^{-3}$, the $\eta^{1/3}$ scaling of growth rates obtained from the present simulation is in agreement with the theory of resistive ballooning modes in stellarators [32]. This suggests that in CFQS plasmas the resistive MHD mode could be the ballooning-type instabilities. A possible stabilization of the ballooning modes due to favourable average curvature effects at low resistivity regimes has also been discussed in [33].

To show the mode structure more clearly, we plot contours of the toroidal electric field in figure 9, where the white dashed line denotes the last closed flux surface. It can be seen that the mode is growing with an initial random perturbation and its structure displays a clear symmetric breaking in the good and bad curvature regions, which is the typical characteristic of the resistive ballooning mode. In addition, it has been found that the spatial location of the mode is closely related to the local pressure gradient (not shown here).

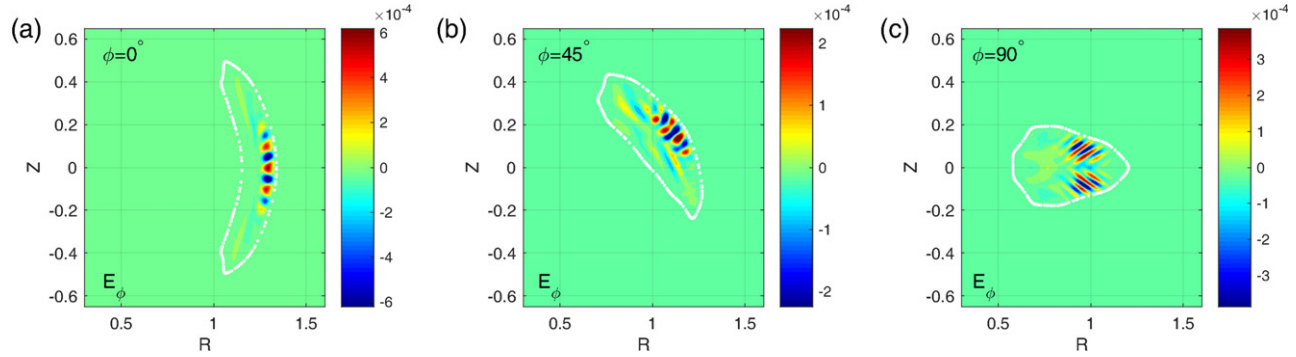

Figure 9. The contours of the toroidal electric field of the mode at three different toroidal angles.

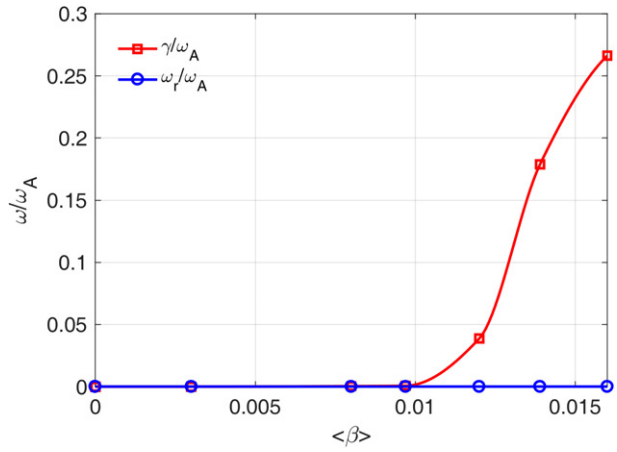

Figure 10. The mode frequency and growth rate as a function of $\langle\beta\rangle$.

To clarify plasma beta effects, we have computed the growth rate and frequency of the modes as a function of $\langle\beta\rangle$. The results are depicted in figure 10. A strong dependence of the growth rate on $\langle\beta\rangle$ is observed along with a zero-mode frequency. This implies that the mode is a pure MHD mode. Note that when the $\langle\beta\rangle$ value exceeds 1.6%, the iota profile might be close to 1/2 (=2/4), for which $n = -2$ is the dominant mode. In the present case, the mode is always dominated by $n = -4$ when $\langle\beta\rangle \leqslant 1.6\%$. Moreover, figure 10 shows that the mode is stable when the $\langle\beta\rangle$ is smaller than $\sim$1%, which suggests a beta limit for the present design of the CFQS. Here, we have to bear in mind that the above beta dependence for the mode growth rate and frequency includes a dependence on toroidal currents. When we change the beta value, the bootstrap current also varies (see figure 4(a)), which may impose an impact on the growth rate and frequency of the modes. The missing values of the growth rate could be roughly estimated by an interpolation in figure 10. It should be noted that, as an important MHD instability in the QAS [28, 34], the ideal external kink mode is not discussed here. This mode might be unstable when the rotational transform at the plasma boundary exceeds 0.5 [28] and, therefore, it should be investigated in the future.

4. Summary

In this paper, the equilibrium with magnetic islands in the CFQS QAS has been calculated by the HINT code. In high beta cases, the impact of magnetic islands on the magnetic axis shift has been discussed. The resistive MHD mode was simulated by the MEGA code for the CFQS. The main results obtained in this paper are summarized as follows.

(a) For the finite plasma beta, the magnetic island chains are generated and a stochastization of magnetic field lines expands with increasing beta values at the plasma boundary. In high beta cases, the outward shift of the magnetic axis is enhanced.

(b) With bootstrap current effects, the low-order islands spread over the whole plasma region, which leads to a shrinkage of nested flux surfaces. Nevertheless, a flat pressure profile can significantly reduce the island width and field line stochastization due to the absence of certain rational surfaces, and hence, the nested flux surfaces can be relatively well maintained.

(c) The simulation of MHD instabilities for the CFQS configuration indicates that the MHD modes are dominated by the resistive ballooning mode with strong mode coupling. A resistivity scaling of the mode growth rate in the QAS, $\gamma \propto \eta^{1/3}$, is also consistent with the theory of resistive ballooning modes.

Acknowledgments

The authors would like to thank Prof. Y. Suzuki and Dr Jie Huang for useful suggestions. This work was supported by the National Natural Science Foundation of China under Grant Nos. 11820101004, 11975188, 11905176, 11947404 and the National Key R & D Program of China under Grant No. 2017YFE0301705 and the Advanced Foreign Expert Introduction Program under Grant No. G20200023025. This work was also supported by the general collaboration research program of the National Institute for Fusion Science through Grant No. NIFS19KBAP051.

ORCID iDs

X.Q. Wang https://orcid.org/0000-0001-8485-895X
Y. Xu https://orcid.org//0000-0003-4882-647X
A. Shimizu https://orcid.org/0000-0003-3764-3184
S. Okamura https://orcid.org/0000-0002-8156-8233
Y. Todo https://orcid.org/0000-0001-9323-8285

H.F. Liu https://orcid.org/0000-0002-0424-645X
H. Liu https://orcid.org/0000-0001-6407-5958

References

[1] Nuehrenberg J. *et al* 1994 *Quasi-Axisymmetric Tokamaks, Theory of Fusion Plasmas Proc. of the Joint Varenna-Lausanne International Workshop, Bologna* (Editrice Compositori) pp 3–12
[2] Xu Y. 2016 *Matter Radiat. Extremes* **1** 192–200
[3] Matsuoka K. *et al* 1997 *Plasma Phys. Rep.* **23** 542
[4] Okamura S. *et al* 2000 *J. Plasma Fusion Res. Ser.* **3** 73
[5] Okamura S. *et al* 2001 *Nucl. Fusion* **41** 1865
[6] Matsuoka K. *et al* 2004 *Fusion Sci. Technol.* **46** 378
[7] Okamura S. *et al* 2004 *Nucl. Fusion* **44** 575
[8] Reiman A. *et al* 1998 *J. Plasma Fusion Res. Ser.* **1** 429 http://www.jspf.or.jp/JPFRS/PDF/Vol1/jpfrs1998_01-429.pdf
[9] Reiman A. *et al* 1999 *Plasma Phys. Control. Fusion* **41** B273
[10] Neilson G.H. *et al* 2000 *Phys. Plasmas* **7** 1911
[11] Zarnstorff M.C. *et al* 2001 *Plasma Phys. Control. Fusion* **43** A237
[12] Drevlak M., Brochard F., Helander P., Kisslinger J., Mikhailov M., Nührenberg C., Nührenberg J. and Turkin Y. 2013 *Contrib. Plasma Phys.* **53** 459
[13] Brochard F. *et al* 2014 *41st EPS Conf. on Plasma Physics* (Berlin June 23–27 2014) P2 081 http://ocs.ciemat.es/EPS2014ABS/pdf/P2.081.pdf
[14] Xu Y. *et al* 2018 Physical and engineering designs for Chinese first quasi-axisymmetric stellarator (CFQS) *2018 IAEA Fusion Energy Conf.* (Gandhinagar) EX/P5-23 https://conferences.iaea.org/event/151/papers/5632/files/5125-IAEA2018_8_pages_Yuhong_XU_final.pdf
[15] Liu H. *et al* 2018 *Plasma Fusion Res.* **13** 3405067
[16] Liu H. *et al* 2021 *Nucl. Fusion* **61** 016014
[17] Shimizu A. *et al* 2018 *Plasma Fusion Res.* **13** 3403123
[18] Isobe M. *et al* 2019 *Plasma Fusion Res.* **14** 3402074
[19] Kinoshita S., Shimizu A., Okamura S., Isobe M., Xiong G., Liu H. and Xu Y.(the CQFS Team) 2019 *Plasma Fusion Res.* **14** 3405097
[20] Hirshman S.P. *et al* 1983 *Phys. Fluids* **26** 3553
[21] Suzuki Y., Nakajima N., Watanabe K., Nakamura Y. and Hayashi T. 2006 *Nucl. Fusion* **46** L19
[22] Isobe M. *et al* 2002 *J. Plasma Fusion Res. Ser.* **5** 360 http://www.jspf.or.jp/JPFRS/PDF/Vol5/jpfrs2002_05-360.pdf
[23] Todo Y. and Sato T. 1998 *Phys. Plasmas* **5** 1321
[24] Suzuki Y. 2017 *Plasma Phys. Control. Fusion* **59** 054008
[25] Suzuki Y. 2020 *Plasma Phys. Control. Fusion* **62** 104001
[26] Okamura S. *et al* 2020 *J. Plasma Phys.* **86** 815860402
[27] Shaing K.C. *et al* 1989 *Phys. Fluids* B **1** 148
[28] Suzuki C. *et al* 2004 *J. Plasma Fusion Res. Ser.* **6** 519 http://www.jspf.or.jp/JPFRS/PDF/Vol6/jpfrs2004_06-519.pdf
[29] Henneberg S.A., Drevlak M., Nührenberg C., Beidler C.D., Turkin Y., Loizu J. and Helander P. 2019 *Nucl. Fusion* **59** 026014
[30] Todo Y., Berk H.L. and Breizman B.N. 2010 *Nucl. Fusion* **50** 084016
[31] Todo Y., Seki R., Spong D.A., Wang H., Suzuki Y., Yamamoto S., Nakajima N. and Osakabe M. 2017 *Phys. Plasmas* **24** 081203
[32] Cooper W.A. and Depassier M.C. 1985 *Phys. Rev.* A **32** 3124
[33] Connor J.W. and Hastie R.J. 1999 *Phys. Plasmas* **6** 4260
[34] Fu G.Y. *et al* 2007 *Fusion Sci. Technol.* **51** 218